Journal of
Marine Science and Engineering

MDPI

Article

Study on the Impact of Tail Wing Profiles on the Resistance Characteristics of Amphibious Vehicles

Zhongyuan Jiang, Jiangming Ding * and Zhourui Li

School of Naval Architecture, Ocean and Energy Power Engineering, Wuhan University of Technology, Wuhan 430063, China; 284534@whut.edu.cn (Z.J.); 349039@whut.edu.cn (Z.L.)
* Correspondence: dingjiangming@whut.edu.cn

Abstract: The resistance performance of amphibious vehicles can be improved by installing underwater tail hydrofoils. The research on the impact of different hydrofoil profiles on the resistance characteristics of amphibious vehicles can provide a reference for the vehicle's design. For an amphibious vehicle model, five shapes of symmetrical hydrofoils, NACA0012, NACA0015, NACA0016, and asymmetric hydrofoils NACA23012, NACA66-209, were selected as the underwater tail wing of the vehicle body, respectively. Based on the RANS method and overset grid technology, the resistance performance of the vehicle body was numerically calculated, and the resistance variation in the amphibious vehicle equipped with different tail hydrofoils at $0.43 < Fr_{\nabla} < 1.3$ speed was obtained. The basic shape of amphibious vehicle tail wings can be determined by comparing the effects of symmetrical hydrofoils and asymmetric hydrofoils on body resistance. The results show that the asymmetric hydrofoils have a better resistance reduction effect on amphibious vehicles than the symmetrical ones. Among them, an amphibious vehicle installing the asymmetric hydrofoil NACA66-209 as an underwater tail wing can reduce resistance by 44.3%. Chord length is an important factor affecting the resistance reduction performance of tail wings. When $Fr_{\nabla} = 1.3$, the asymmetric hydrofoil optimized based on chord length has a 21.2% higher resistance reduction effect on amphibious vehicles.

Keywords: amphibious vehicles; resistance; tail wing; hydrofoil parameter optimization; CFD

Citation: Jiang, Z.; Ding, J.; Li, Z. Study on the Impact of Tail Wing Profiles on the Resistance Characteristics of Amphibious Vehicles. *J. Mar. Sci. Eng.* **2024**, *12*, 780. https://doi.org/10.3390/jmse12050780

Academic Editor: Md Jahir Rizvi

Received: 9 April 2024
Revised: 1 May 2024
Accepted: 4 May 2024
Published: 7 May 2024

1. Introduction

Amphibious vehicles, which combine features of both automobiles and ships, are primarily utilized for operations such as amphibious transport, rescue missions, and beach landings, where mobility and speed are crucial. Consequently, enhancing the speed and efficiency of amphibious vehicles to meet the high demands for rapid water transportation has emerged as a significant research interest globally. A promising approach for reducing resistance and improving speed involves the adoption of resistance-reducing devices, including skates, wave plates, and hydrofoils, which has garnered considerable attention in the design of amphibious vehicles.

Kemp et al. [1] conducted experiments on the AAAV amphibious vehicle outfitted with skates positioned at the front, rear, and along the body. Their findings indicated that skates enable the vehicle to achieve a gliding state more swiftly, thereby reducing resistance and enhancing speed effectively. Latorre and Arana [2] examined the resistance characteristics of an amphibious vehicle equipped with a bow wave pressure plate at high speeds, demonstrating that the plate significantly improves the wave pressure effect and reduces vehicle trim, thus optimizing resistance performance under high-speed conditions. Yu et al. [3] explored the impact of different combinations of angles for skates mounted on the front and rear of the vehicle body on the resistance-to-lift ratio, employing orthogonal experimental design and numerical simulation. Their research identified an optimal angle combination for the skates, optimizing performance through analytical methods.

Further studies by Sun et al. [4] focused on how the length and mounting angle of the tail pressure plate affect the vehicle's resistance performance and navigational stability. Du et al. [5] investigated the effects of wave pressure plates on the motion stability of high-speed amphibious platforms, employing the SVM classification algorithm to generate a stability response surface. This analysis facilitates the determination of the amphibious vehicle's maximum speed and the tail wave plate's optimal angle range to maintain stability at peak velocities. Peng et al. [6] assessed the impact of tail plates on the resistance characteristics of wheeled amphibious vehicles, finding that a single tail plate offers superior resistance reduction compared with double tail plates, albeit increasing overall body resistance beyond certain speeds. Lastly, Lee et al. [7] utilized the NACA0012 profile for the hydrofoil of an amphibious vehicle's underwater tail wing, which effectively adjusts the vehicle's trim. Within specific installation angles, a larger angle yields better trim adjustment and consequently more pronounced resistance improvement.

In recent studies, it has been demonstrated that installing stern flaps and underwater tail hydrofoils on amphibious vehicles can significantly enhance wave compression and resistance reduction [8–12]. Both these additions are instrumental in adjusting the vehicle's attitude and optimizing the flow field around the vehicle's hull [13]. The stern flap, affixed to the vehicle's bottom plate, provides a static method of attitude adjustment [14]. Unlike the more versatile underwater tail hydrofoils, the stern flap's position is fixed, offering limited adjustability primarily through alterations in its length and downward angle. This restricts its impact on lifting the vehicle's body. Moreover, during navigation, the stern flap is subject to considerable stress concentration from wave pressure and water resistance, potentially compromising the vehicle's structural strength.

In contrast, the unique hydrodynamic profile of underwater tail hydrofoils not only mitigates wave pressure but also leverages the wake to generate additional thrust, further reducing resistance. Current research predominantly explores the effects of front and rear flaps on the navigational attitude of amphibious vehicles and their combined resistance-reduction efficacy. However, investigations into the resistance-reduction capabilities of underwater tail wings remain limited. The selection and application of hydrofoil profiles in these studies are often simplistic, offering scant guidance for the design of amphibious vehicle tail wings due to a dearth of comparative analyses [15,16].

Adjusting underwater tail hydrofoils' position and orientation is crucial for reducing amphibious vehicles' navigational resistance [17]. The effectiveness of these adjustments depends on the hydrofoil's shape, necessitating initial design considerations of its geometry for optimal resistance reduction. However, existing research on tail wing designs lacks in-depth comparative and quantitative analysis, offering limited guidance for the preliminary design phase. Addressing this gap by exploring how various tail wing shapes affect resistance is essential, aiming to establish a guiding preliminary design for an amphibious vehicle tail that significantly improves the resistance reduction effect.

In this paper, symmetrical hydrofoil NACA0012, NACA0015, NACA0016, and asymmetric hydrofoil NACA23012 and NACA66-209 are selected as the underwater tail wing of the vehicle body, and the resistance of the vehicle body is calculated numerically. Among them, the symmetric wing shape NACA0012 is the tail wing shape used in most of the hydrodynamic performance studies of amphibious vehicles, and the wing shapes of NACA0015 and NACA0016 are similar to the shape of NACA0012 but with the thicknesses increasing sequentially, which can reflect the effect of the tail thicknesses on the drag force of amphibious vehicles by comparing the drag reduction effect of these three wing shapes. Asymmetric hydrofoils NACA23012 and NACA66-209, common in high-speed amphibious vehicles, offer insights into asymmetric design benefits.

By comparing the resistance reduction effects of symmetrical hydrofoils and asymmetric hydrofoils on amphibious vehicles, the hydrofoil with better hydrodynamic performance is selected as the initial underwater tail wing shape. Based on it, the hydrofoil's chord length parameter is optimized. The research results of this paper can provide a reference for the design of resistance-reduction components for amphibious vehicles.

Future work should expand on hydrofoil variety and include experimental validation to refine these findings.

2. Numerical Simulation Method and Verification

2.1. Geometric Model

The amphibious vehicle model employed in this study is depicted in Figure 1. The design of the vehicle's body is rectangular, with a wave board mounted at the front, inclined at 22° to the horizontal, aimed at mitigating wave resistance. The dimensions of the vehicle include a length (L), width (B), and draft (T), resulting in a body aspect ratio (L/B) of 3.43 and a width-to-draft ratio (B/T) of 7.35.

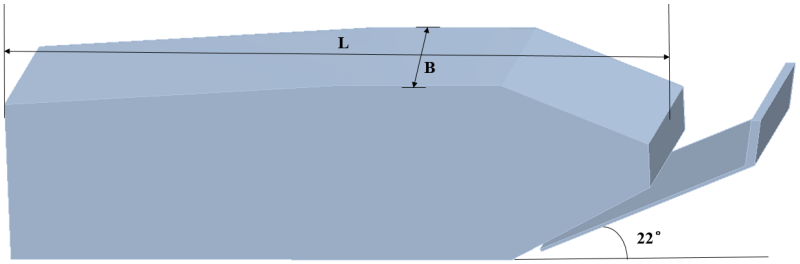

Figure 1. Amphibious vehicle model.

Five hydrofoils were evaluated for their suitability as the underwater tail wing structure of the amphibious vehicle: three symmetric hydrofoils (NACA0012, NACA0015, NACA0016) and two asymmetric hydrofoils (NACA23012 and NACA66-209). The profiles of each hydrofoil are depicted in Figure 2. Taking NACA0012 as a representative example, the installation specifics are illustrated in Figure 3. The tail hydrofoil's rear end is positioned at a horizontal distance of 0.477B from the vehicle's rear transom plate, and it is elevated 0.05B vertically from the underbody, angled at 2° relative to the incoming flow direction. The chord length for all selected hydrofoil profiles is consistent at 0.469B, and they share the same installation parameters.

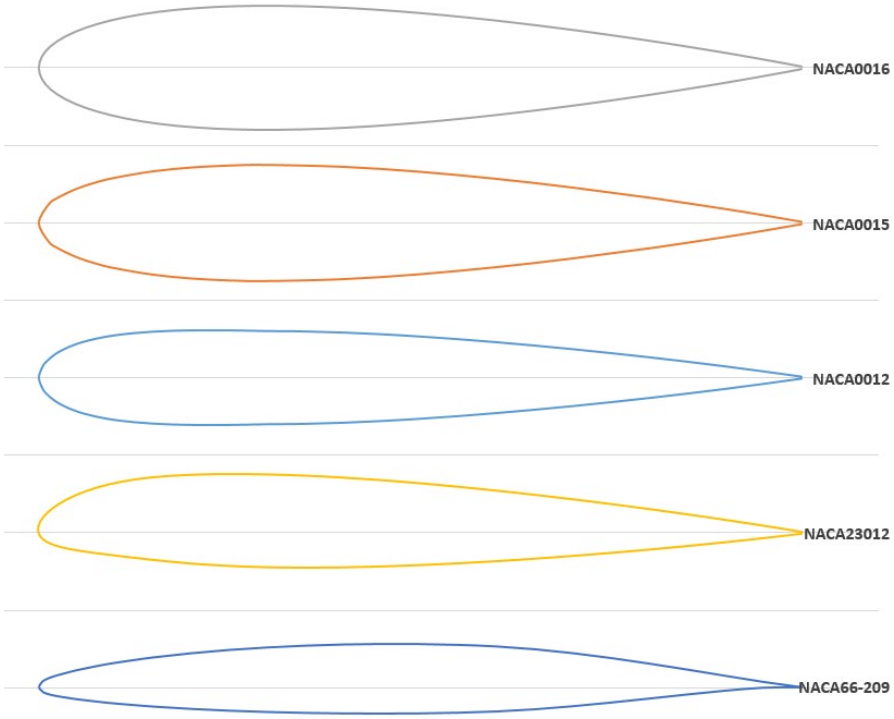

Figure 2. Profiles of tail wing.

Figure 3. Installation position of the tail wing.

2.2. Numerical Simulation Method

In this paper, the hydrostatic resistance characteristics of amphibious vehicles are calculated based on CFDs commercial software STAR-CCM+13.02. Supposing the fluid flowing around the vehicle body is a viscous incompressible fluid, and the flow satisfies the law of conservation of mass and conservation of momentum [18,19]. The hydrodynamic performance of the amphibious vehicle was solved by the RANS equation, and the Realizable k-ε turbulence model fitting for complex geometric external flows was selected for the solution of the RANS equation. The governing equation and turbulence equation used in the calculation are as follows:

The governing equation is expressed in Equation (1).

$$\frac{\partial(\rho u_i)}{\partial x_i} = 0 \frac{\partial(\rho u_i)}{\partial t} + \frac{\partial(\rho u_i u_j)}{\partial x_i} = -\frac{\partial p}{\partial x_i} + \frac{\partial}{\partial x_j}(v\frac{\partial u_i}{\partial x_j} - \rho\overline{u_i' u_j'}) + f_i \tag{1}$$

where ν is the kinematic viscous coefficient, $\rho\overline{u_i' u_j'}$ is the Reynolds stress term, f_i is the fluid mass force.

The realizable k-ε turbulence model is expressed in Equation (2).

$$\frac{\partial(\rho k)}{\partial t} + \frac{\partial(\rho k u_i)}{\partial x_i} = \frac{\partial}{\partial x_j}\left[(\mu + \frac{\mu_i}{\sigma_k})\frac{\partial k}{\partial x_j}\right] + G_k - \rho\varepsilon\frac{\partial(\rho\varepsilon)}{\partial t} + \frac{\partial(\rho\varepsilon u_i)}{\partial x_i} = \frac{\partial}{\partial x_j}\left[(\mu + \frac{\mu_i}{\sigma_\varepsilon})\frac{\partial \varepsilon}{\partial x_j}\right] + \rho C_1 E\varepsilon - \rho C_2 \frac{\varepsilon^2}{k + \sqrt{\nu\varepsilon}} \tag{2}$$

where C_1 and C_2 are empirical constants, and σ_k and σ_ε are Prandtl numbers corresponding to the turbulent kinetic energy k and the turbulent dissipation rate ε, respectively. ν is the kinematic viscosity coefficient, and G_k expresses the turbulence kinetic energy due to mean velocity gradients.

The flow governing equations are discretized using the finite volume method, with the Volume of the Fluid method employed to capture the free surface dynamics [20]. The Dynamic fluid–body interaction approach is utilized to simulate the motion of the vehicle body, allowing for the degrees of freedom in longitudinal rotation and vertical translation. To address the significant changes in vehicle attitude during navigation, the overset grid technique is applied. The selection of the time step, critical for the accuracy and stability of the simulation, follows the guidelines recommended by the International Towing Tank Conference for numerical simulation of ship resistance [21]. The equation for determining the time step, which involves the length between perpendiculars (L_{PP}) of the boat body and the speed (U), is presented in Equation (3):

$$\Delta t = (0.005 \sim 0.01) L_{pp} / U \tag{3}$$

2.3. Verification of Numerical Simulation Method

The volume Froude number Fr_∇ is taken as a dimensionless number representing the sailing speed of the amphibious vehicle in Equation (4).

$$Fr_\nabla = \frac{U}{\sqrt{g\nabla^{1/3}}} \tag{4}$$

where U is the velocity of the vehicle, and g is the gravitational acceleration; ∇ is the displacement volume.

A validation study using the DTMB5415 ship model was conducted to verify the computational approach. The DTMB5415, a medium-high-speed vessel, exhibits behavior analogous to the amphibious vehicle across the studied Froude number range ($0.43 < Fr_\nabla < 1.3$). This range includes both displacement navigation ($0.43 < Fr_\nabla < 1$) with minimal attitude changes and a transitional state ($1 < Fr_\nabla < 1.3$) with significant attitude adjustments. The DTMB5415 model, whose dimensions include a length (L_1 = 5.72 m), a width (B_1 = 0.76 m), a draft (T_1 = 0.248 m), and a displacement (Δ_1 = 549 kg), is shown in Figure 4. The CFDs commercial software STAR-CCM+ is used to calculate the resistance performance of the boat at the speed V_1 = 2.097 m/s, and the time step taken is 0.005 L_1/V_1.

Figure 4. The ship model of DTMB5415.

The numerical simulations leverage a half-ship computational domain. Due to the hull symmetry, the essential flow field features around the hull are mirrored in the half-ship model. Thus, employing a half-ship computational domain for hull resistance calculations can minimize computational mesh requirements and computation time.

The computational domain comprises a stationary background and a dynamic overset domain. The background domain boundaries are set as follows: entrance boundary at 1 L_1 from the bow, outlet boundary at 5 L_1 from the stern, and top and bottom boundaries at 0.67 L_1 and 1.75 L_1 from the hull, respectively, and the side boundary at 2 L_1 from the mid-longitudinal profile. Boundary conditions include a pressure outlet, a symmetry plane along the mid-longitudinal profile, velocity inlets for other boundaries, and a nonslip wall condition for the hull surface. Wave reflection is minimized by damping zones extending 1 L_1 at the outlet, inlet, and side boundaries. The overset domain is a rectangular region with dimensions of 1.4 L_1 in length, 2 B_1 in width, and 0.3 L_1 in height, as detailed in Figure 5.

The computational domain employs a trimmed grid mesh, supplemented by a prism layer mesh to accurately delineate the boundary layer flow along the hull surface. Mesh refinement is applied to the free surface, Kelvin wave region, and overset grid areas to enhance simulation precision. The completed mesh comprises a total of 1.32 million cells, with the detailed mesh refinement process illustrated in Figure 6.

The numerical results for the DTMB5415 hull at a velocity of V_1 = 2.097 m/s were compared with experimental data from the INSEAN pool in Italy, as detailed in Table 1. The discrepancy between the Computational Fluid Dynamics (CFDs) calculations and the experimental findings (EFDs) is confined to about 5%. This comparison validates the accuracy of the employed numerical method in estimating the hydrodynamic resistance of the hull, demonstrating its applicability for assessing the navigational resistance of amphibious vehicles.

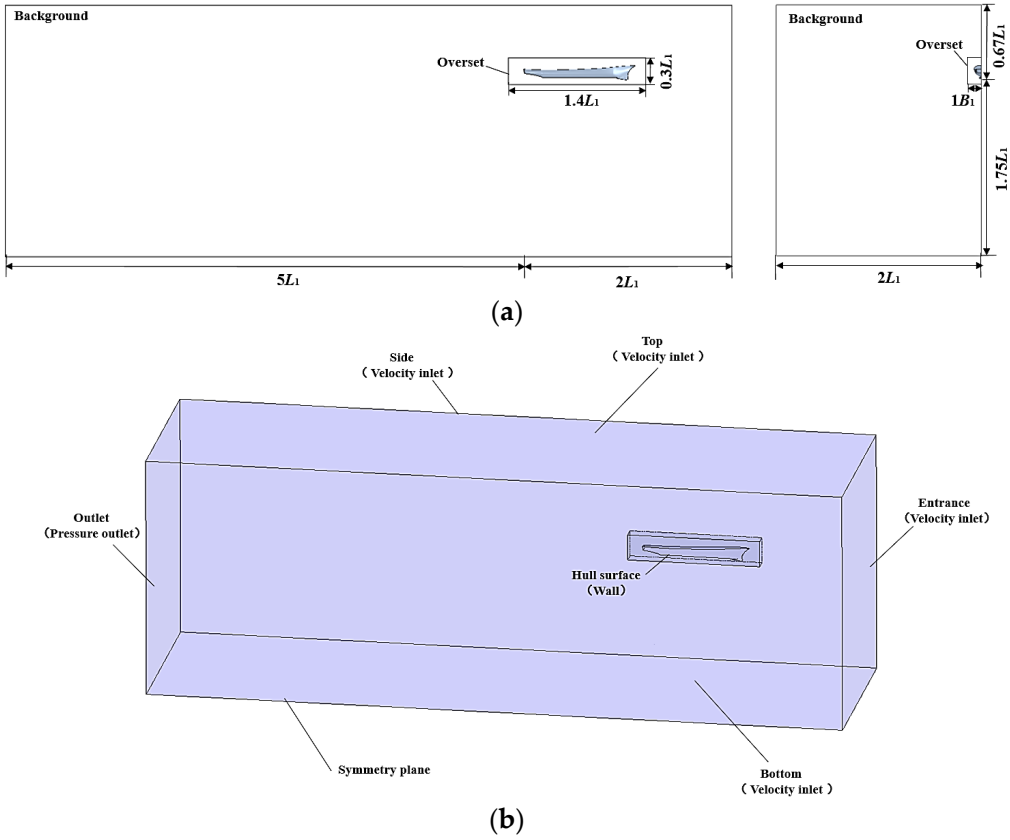

Figure 5. The computational domain division and boundary conditions: (**a**) the computational domain division; (**b**) the boundary conditions.

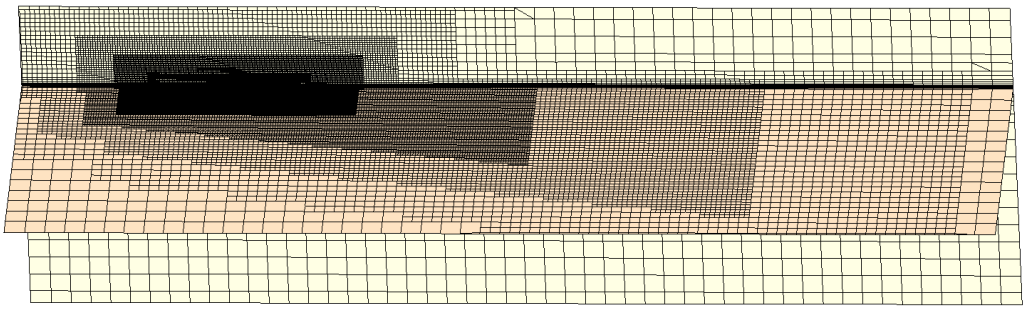

Figure 6. Mesh refining.

Table 1. The resistance calculation results of DTMB5415.

Method	EFDs (INSEAN)	CFDs
Resistance (N)	46.05	48.48

2.4. Numerical Simulation of Resistance on Amphibious Vehicle and Grid Convergence Analysis

Based on the DTMB5415 hull resistance numerical simulation method, the resistance of an amphibious vehicle without a tail wing is calculated at the design speed with a Froude number (Fr_∇) of 1.08. The mesh division of the amphibious vehicle is shown in Figure 7. The setup for boundary conditions and computational domain gridding employed for the amphibious vehicle is similar to the DTMB5415 hull analysis.

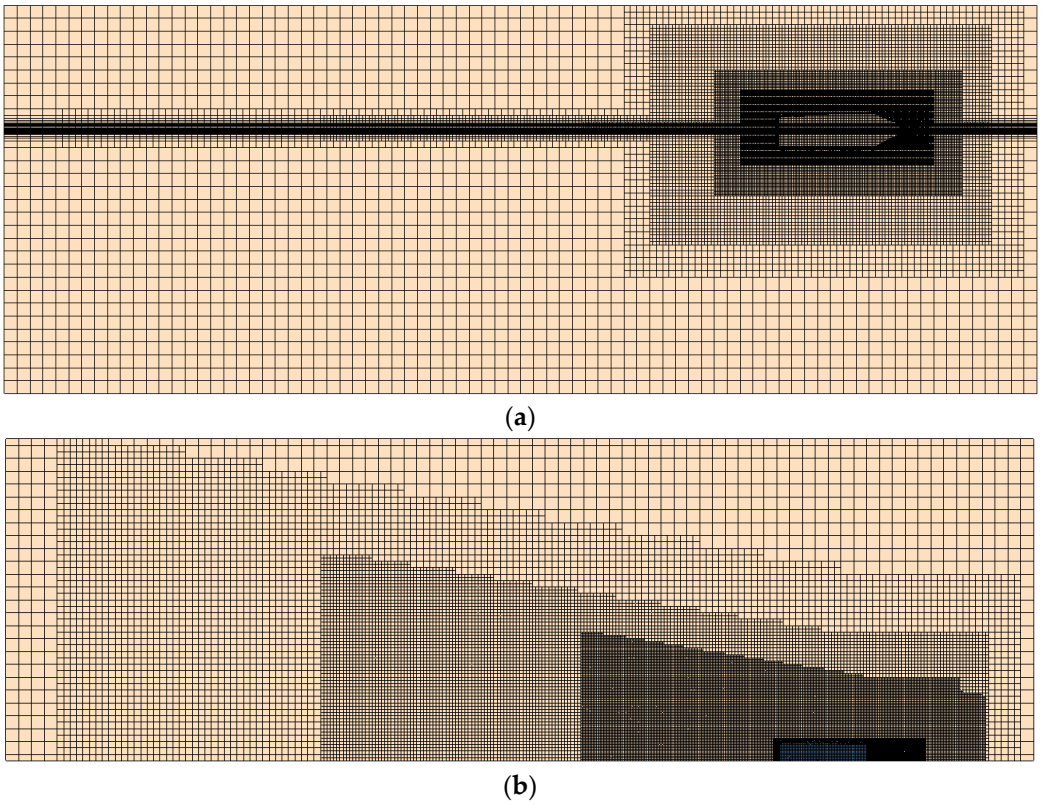

Figure 7. Grid division of the amphibious vehicle: (**a**) amphibious vehicle computational domain gridding; (**b**) free surface refining of amphibious vehicle.

To validate the accuracy of the numerical calculation method for the amphibious vehicle and the reasonableness of the computational domain's grid division, a grid convergence analysis was conducted using three sets of grids G_1, G_2, and G_3 with different densities (fine, medium, and coarse) defined by a mesh refinement ratio ($r_G = \sqrt{2}$) between the series of grid schemes. The specific parameters for each grid set are detailed in Table 2.

Table 2. The resistance calculation results of each grid scheme.

Grid Scheme	Base Size (m)	Grid Number (10^4)	R_t/Δ
G_1	0.088	556	0.187
G_2	0.125	223	0.185
G_3	0.177	93	0.198

The simulation results of the vehicle resistance are converted into a unit displacement resistance (S) expressed in Equation (5).

$$S = R_t/\Delta \tag{5}$$

where R_t represents the vehicle resistance; Δ represents the vehicle displacement.

The results of resistance calculation under each grid scheme are shown in Table 2, the resistance results of different grid schemes G_1, G_2, and G_3 are represented by S_1, S_2, and S_3, respectively. The grid convergence rate $R_G = |(S_2 - S_1)/(S_3 - S_2)| = 0.154$, $0 < R_G < 1$ reveals that the calculation grid monotonically converges, suggesting that the G_2 grid scheme strikes an optimal balance between accuracy and computational efficiency for the numerical calculation of amphibious vehicle resistance.

For the amphibious vehicle resistance calculation under the G_2 grid scheme, time steps of t = 0.005 s, 0.01 s, and 0.02 s were tested. The results, detailed in Table 3, show relative deviations of 0.0081% for t_2 = 0.01 s and −0.0835% for t_3 = 0.02 s from the t_1 = 0.005 s

benchmark. These findings indicate minimal sensitivity to the time step, with convergence achieved at t_2 = 0.01 s. Thus, t_2 = 0.01 s is identified as the optimal time step for ensuring computational efficiency and accuracy in amphibious vehicle resistance calculations.

Table 3. The resistance calculation results of each time step.

Time Step Scheme	Time Step (s)	R_t/Δ	Relative Deviations (%)
t_1	0.005	0.18503	--
t_2	0.01	0.18505	0.0081%
t_3	0.02	0.18488	−0.0835%

3. Results and Discussion

3.1. Resistance Reduction Effect of Different Tail Wing Hydrofoil Profiles

Fixing the bow plate angle and the center of gravity of the vehicle, a comparison of the CFDs numerical calculation results of the amphibious vehicle installed with different hydrofoils (NACA0012, NACA0015, NACA0016, NACA23012, and NACA66-209) as the underwater tail wings across a speed range of $0.43 < Fr_\nabla < 1.3$ is shown in Figure 8.

The impact of various hydrofoil designs on the resistance performance of amphibious vehicles has distinct trends emerging across different Fr_∇ regions. Taking the resistance of the amphibious vehicle without tail wings as a reference, Table 4 illustrates the resistance percentage change for each hydrofoil design, where positive values denote an increase in resistance, and negative values signify a reduction.

Table 4. The percentage increase in resistance of amphibious vehicles installed with different hydrofoil shapes.

Hydrofoil Profile	Fr_∇ = 0.43	Fr_∇ = 0.57	Fr_∇ = 0.77	Fr_∇ = 1.08	Fr_∇ = 1.3
NACA0012	9.1	4.8	1.9	−14.6	−39.6
NACA0015	9.1	9.5	1.9	−11.9	−35.9
NACA0016	9.1	9.5	0	−10.8	−35.3
NACA23012	18.2	9.5	5.6	−16.2	−42.4
NACA66-209	9.1	9.5	1.9	−17.3	−44.3

For Fr_∇ values below 0.9, the vehicle operates in a displacement state where the addition of tail wings invariably leads to an increase in hydrodynamic resistance. This effect is more pronounced at lower speeds; specifically, at Fr_∇ = 0.43, the incorporation of hydrofoils results in a resistance increase of up to 18.2%. Consequently, amphibious vehicles should retract their tail wings during low-speed navigation to mitigate this adverse effect on resistance. Conversely, in the high-speed regime where Fr_∇ exceeds 0.9, the vehicle transitions towards gliding. During this state, the installation of underwater tail wings contributes positively by reducing resistance. The efficacy of this reduction escalates with increasing speed, culminating in a notable decrease in resistance of over 35% at Fr_∇ = 1.3. This observation underscores the utility of hydrofoils in enhancing the hydrodynamic efficiency of amphibious vehicles, particularly at higher speeds.

Figure 8b,c demonstrates the sinkage and trim of the amphibious vehicle with and without mounted tail wings. Analyzing the amphibious vehicle's behavior reveals that without hydrofoils, it tends to sink, a tendency that initially increases with speed but then lessens due to hydrodynamic lift at higher speeds. Installing tail wings changes this pattern, especially at lower speeds ($Fr_\nabla < 0.9$), where they cause a slight lift, adjusting the vehicle's attitude. As speed increases, this lifting effect is significantly enhanced by the tail wings, culminating at Fr_∇ = 1.3, where most of the hull is lifted out of the water. This demonstrates the effectiveness of hydrofoils in both preventing sinking at lower speeds and achieving greater lift at higher speeds, optimizing the vehicle's performance across different speeds.

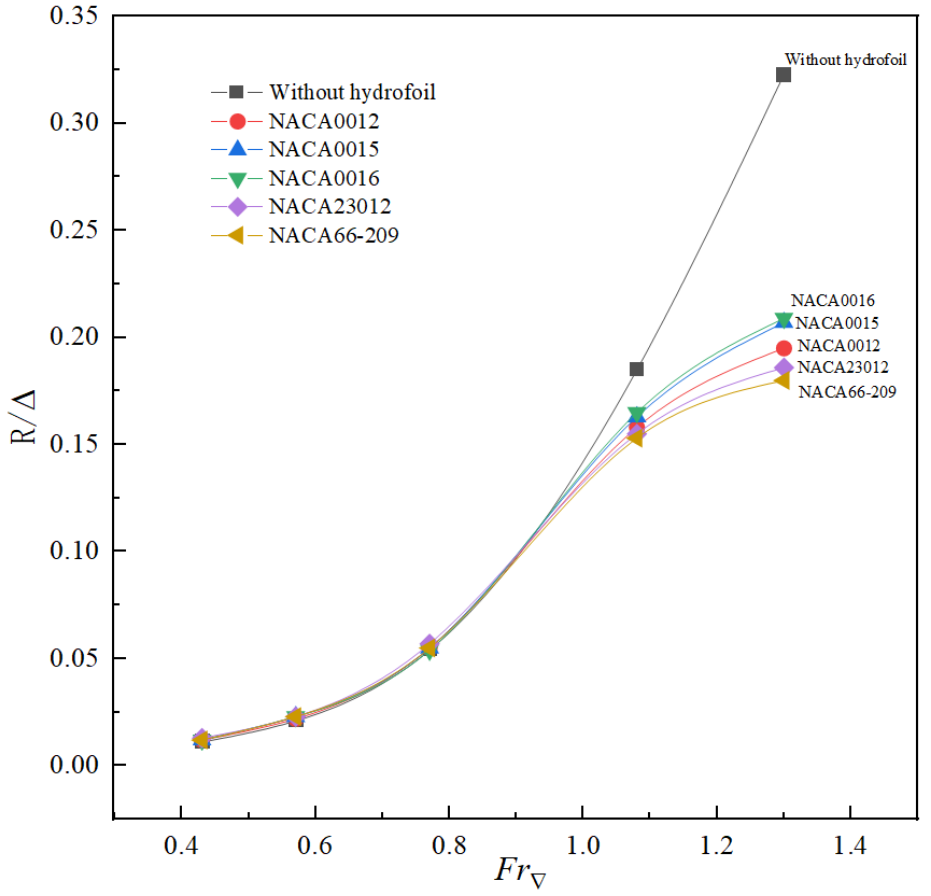

(**a**)

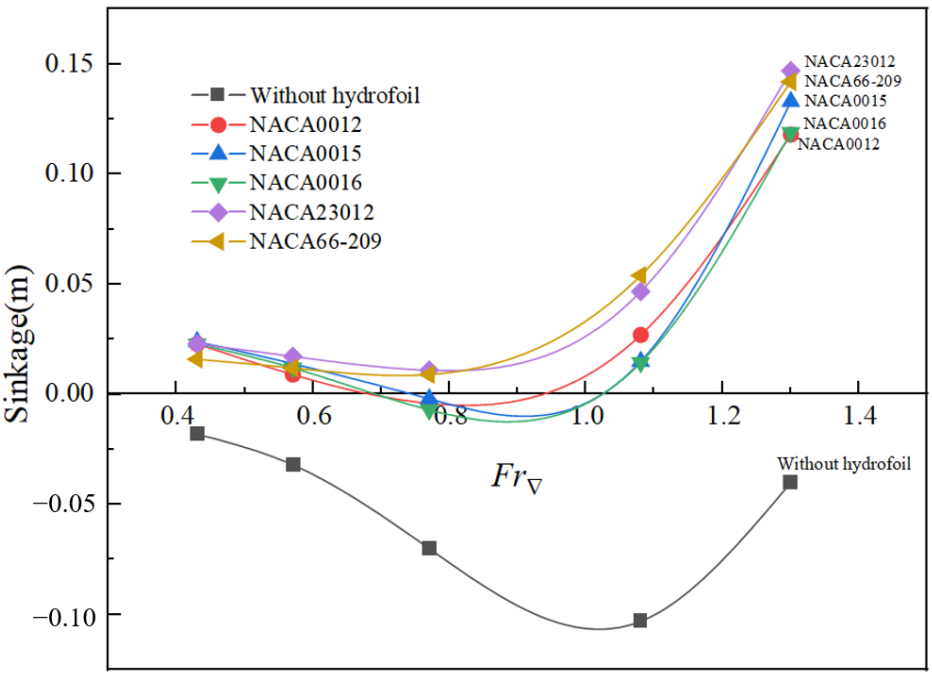

(**b**)

Figure 8. *Cont.*

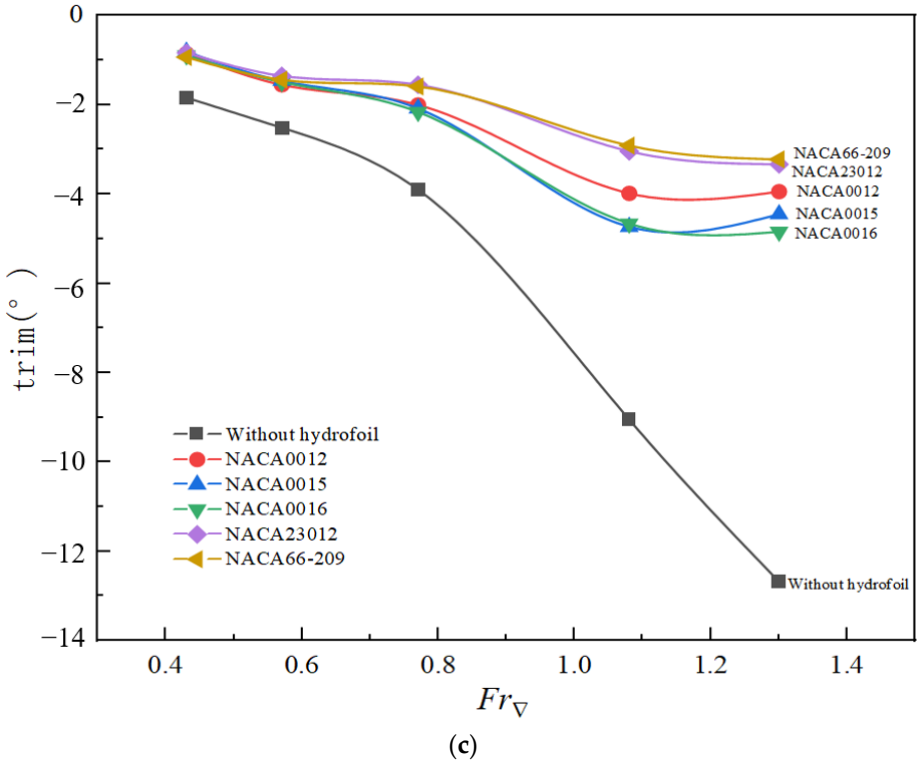

(**c**)

Figure 8. The resistance performance of the amphibious vehicle installed with different hydrofoil shapes: (**a**) resistance; (**b**) sinkage; (**c**) trim.

Due to the lifting effect of hydrodynamic force during navigation, the bow of the amphibious vehicle is gradually lifted out of the water, causing the vehicle to tilt aft. Without a tail hydrofoil, this tail inclination increases with speed, especially when Fr_∇ exceeds 0.9, showing a linear increase in the tail inclination angle. After the amphibious vehicle is installed with a tail hydrofoil, the change in the tail inclination of the vehicle body gradually flattens with the increase in cruising speed, and the angle of the tail inclination is smaller than that of the vehicle without hydrofoil. With the installation of tail wings, the vehicle's tail inclination increases more gradually with speed, and the inclination angle remains smaller. When $Fr_\nabla > 1$, vehicles equipped with tail wings transition into the gliding state more swiftly, and the tail inclination's change levels off, indicating a more stable and efficient navigation attitude.

In evaluating the resistance reduction capabilities of different hydrofoil profiles on amphibious vehicles, it was found that symmetric hydrofoils (NACA0012, NACA0015, NACA0016) lead to diminished resistance performance as their thickness increases, particularly at Fr_∇ greater than 1. This indicates that thicker symmetric hydrofoils are less effective in reducing resistance during higher-speed transitions. On the other hand, asymmetric hydrofoils (NACA23012 and NACA66-209) improve resistance reduction by 3–9% over symmetric ones. However, using NACA23012 at low speeds results in a significant resistance increase of up to 18.2%, the least favorable outcome during displacement navigation.

Conversely, NACA66-209 exhibits a similar increase in resistance at low speeds as symmetric hydrofoils but delivers the highest resistance reduction, up to 44.3%, at medium and high speeds. This analysis reveals the nuanced impact of hydrofoil design on amphibious vehicle performance, suggesting that asymmetric hydrofoils, particularly NACA66-209, are more efficient for reducing resistance at higher operational speeds, despite slight drawbacks at lower speeds.

Table 5 presents the variations in trim and sinkage upon installing different tail wing shapes. Here, positive values in sinkage changes indicate a lifted elevation of the vehicle's

body, and positive trim changes suggest a decrease in the vehicle's tail inclination angle, with the conditions of the vehicle without tail wings serving as the baseline.

Table 5. The changes in sinkage and trim of amphibious vehicles installed with different hydrofoil shapes.

Program	Hydrofoil Profile	Fr_{∇} = 0.43	Fr_{∇} = 0.57	Fr_{∇} = 0.77	Fr_{∇} = 1.08	Fr_{∇} = 1.3
Sinkage (m)	NACA0012	0.041	0.041	0.066	0.13	0.158
	NACA0015	0.042	0.046	0.068	0.118	0.173
	NACA0016	0.041	0.044	0.063	0.1175	0.159
	NACA23012	0.041	0.0493	0.081	0.1497	0.187
	NACA66-209	0.034	0.044	0.079	0.157	0.182
Trim (°)	NACA0012	0.99	0.96	1.9	5.07	8.74
	NACA0015	1.03	1.05	1.82	4.32	8.23
	NACA0016	0.95	1.02	1.74	4.39	7.84
	NACA23012	1.01	1.16	2.35	6.01	9.35
	NACA66-209	0.91	1.07	2.31	6.14	9.46

Table 5's comparison of trim and sinkage across different tail wing shapes reveals that asymmetric hydrofoil shapes, specifically NACA23012 and NACA66-209, are superior in optimizing the amphibious vehicle's sailing attitude compared with symmetric designs. Vehicles equipped with these asymmetric hydrofoils achieve greater lift and exhibit reduced tail trim angles. Consequently, in medium to high-speed conditions, such vehicles experience less resistance due to smaller drainage volumes, benefit from enhanced lift, and encounter reduced navigational resistance.

3.2. The Flow Field Characterization of Asymmetric and Symmetric Hydrofoils

As can be seen from the results of different tail wings on amphibious vehicle's resistance performance in Figure 8, the resistance trends of similar hydrofoils are close to each other, with NACA0012 in symmetric airfoils having a more obvious resistance reduction effect, and NACA66-209 in asymmetric hydrofoils being able to achieve a better resistance reduction effect in high-speed working conditions. Therefore, taking NACA0012 and NACA66-209 as examples to analyze the resistance reduction effect of the tail wing on amphibious vehicles can more clearly summarize the difference in resistance reduction performance between symmetric and asymmetric hydrofoils. In comparing amphibious vehicles equipped with asymmetric NACA66-209 and symmetric NACA0012 hydrofoils across speeds (Fr_{∇} = 0.43, Fr_{∇} = 0.77, and Fr_{∇} = 1.3), this study discerned the influence of hydrofoil geometry on the vehicle's performance, particularly in terms of the hydrodynamics and flow fields shown in Figures 9 and 10.

At a lower speed (Fr_{∇} = 0.43), the impact of hydrofoil design—whether asymmetric like NACA66-209 or symmetric like NACA0012—on the flow field surrounding the vehicle is minimal. This changes as speeds increase, with the symmetric NACA0012 hydrofoil generating a notably larger air cavity behind the vehicle at medium and high speeds. Effectively reducing resistance by "virtually length" lengthening the vehicle in hydrodynamic terms to decrease water contact areas.

While the larger air cavity associated with the NACA0012 hydrofoil at a high speed (Fr_{∇} = 1.3) aids in diminishing resistance, the NACA66-209 hydrofoil's design triggers a more substantial lifting force, leading to a reduced tail trim angle and lower draft. This results in less resistance due to a smaller drainage volume, ultimately making the NACA66-209 more effective in reducing resistance at higher speeds compared with the NACA0012 hydrofoil.

The analysis of pressure distribution on the vehicle bottom with and without tail wings shown in Figure 11 under various speeds indicates that tail wings enhance lift, leading to a shallower draft and reduced bottom pressure. Figure 12 shows the pressure distribution on the upper surface of NACA0012 and NACA66-209 in typical speed conditions.

At a low speed (Fr_{∇} = 0.43), the symmetric hydrofoil NACA0012 shows a greater high-pressure area compared with the asymmetric hydrofoil NACA66-209, resulting in a

more pronounced pressure difference and thus a shallower draft and smaller tail inclination. However, at this speed, the overall resistance difference between models is minimal due to similar wave conditions and displacement navigation.

When Fr_{∇} = 0.77, the pressure difference is more significant for the asymmetric NACA66-209, providing greater lift and resulting in a smaller draft and tail inclination than with the NACA0012. As speed increases, the wave resistance effect intensifies, but the enhanced lift from the tail wings helps to mitigate resistance increases, with both hydrofoil types showing similar effects on resistance.

At a high speed (Fr_{∇} = 1.3), the vehicle enters the gliding state gradually, with resistance mainly from wave generation. Here, the asymmetric hydrofoil NACA66-209, with its larger pressure difference between surfaces, offers greater tail lift, improving the vehicle's sailing attitude and reducing resistance more effectively than the symmetric hydrofoil NACA0012.

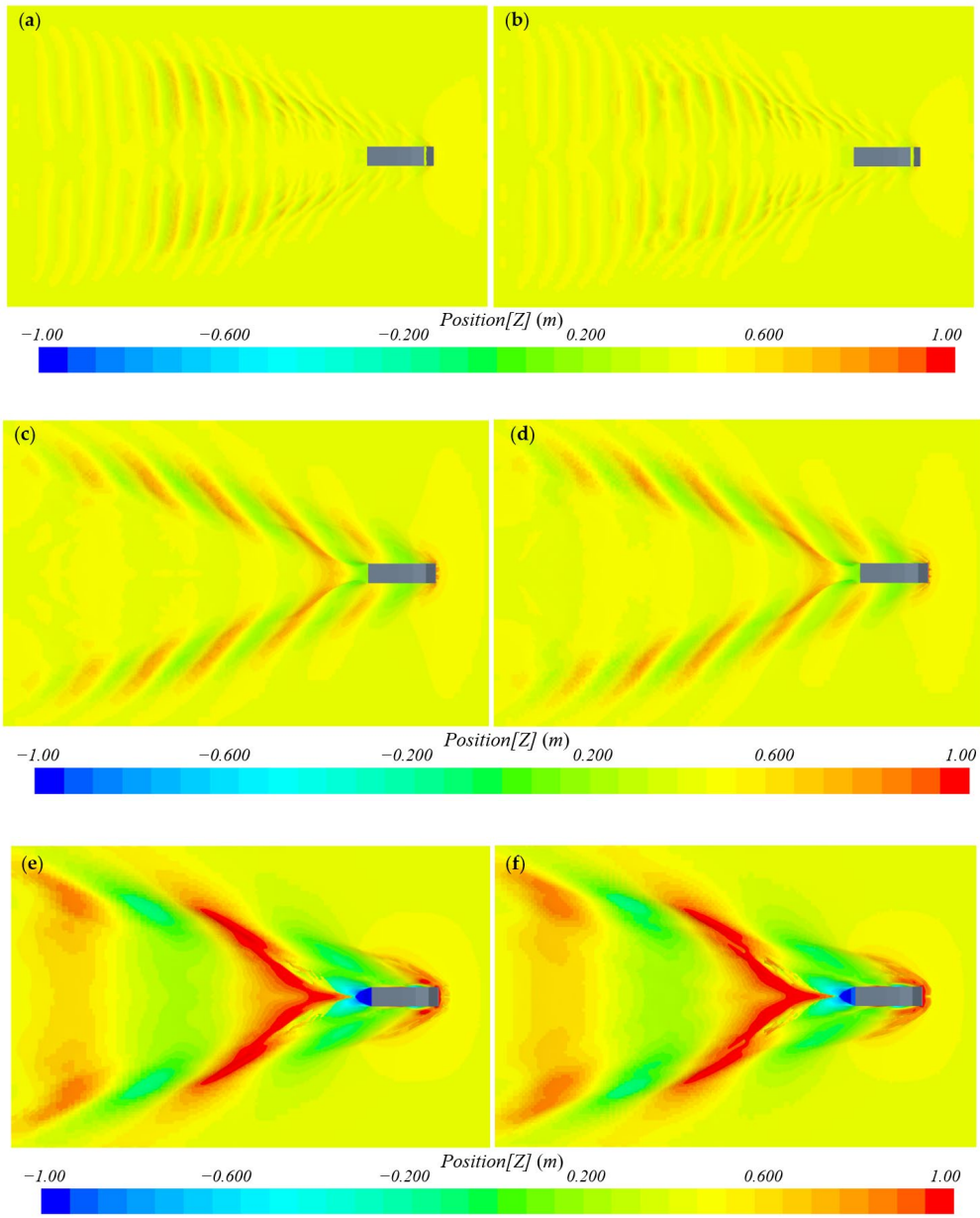

Figure 9. The free surface of typical speed conditions: (**a**) NACA0012 Fr_{∇} = 0.43; (**b**) NACA66-209 Fr_{∇} = 0.43; (**c**) NACA0012 Fr_{∇} = 0.77; (**d**) NACA66-209 Fr_{∇} = 0.77; (**e**) NACA0012 Fr_{∇} = 1.3; (**f**) NACA66-209 Fr_{∇} = 1.3.

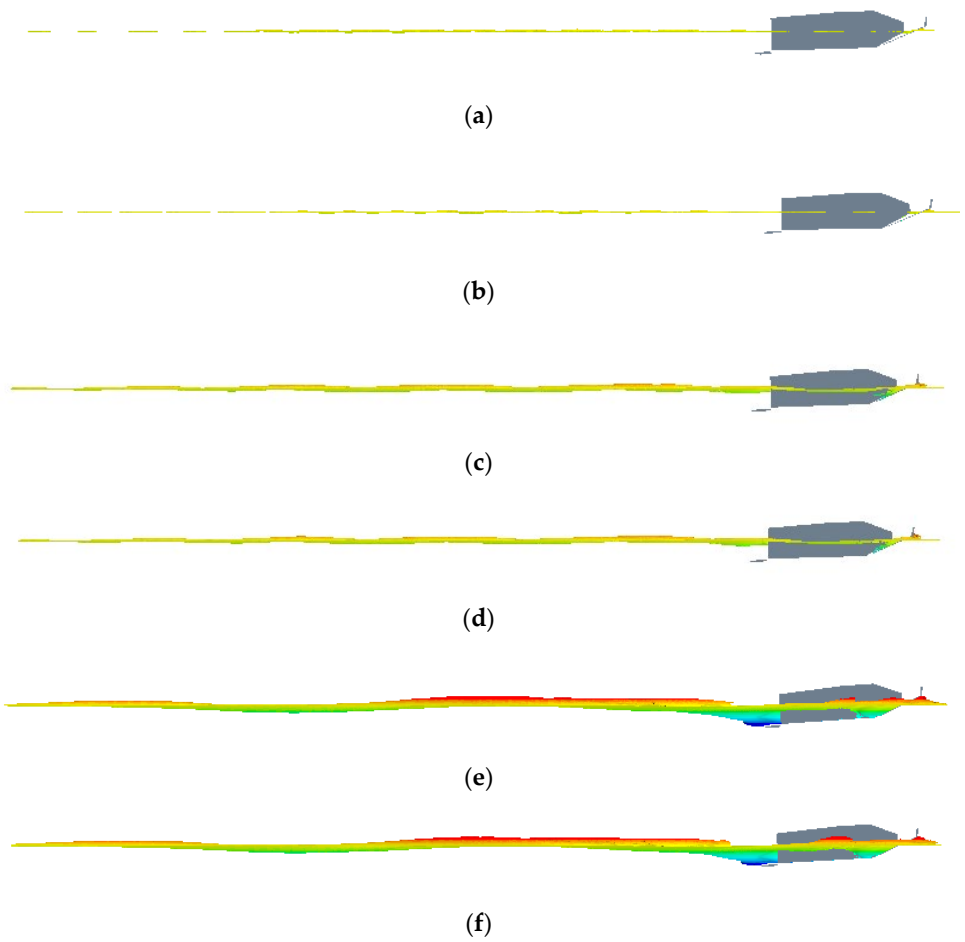

Figure 10. The vehicle water line of typical speed conditions: (**a**) NACA0012 Fr_{∇} = 0.43; (**b**) NACA66-209 Fr_{∇} = 0.43; (**c**) NACA0012 Fr_{∇} = 0.77; (**d**) NACA66-209 Fr_{∇} = 0.77; (**e**) NACA0012 Fr_{∇} = 1.3; (**f**) NACA66-209 Fr_{∇} = 1.3.

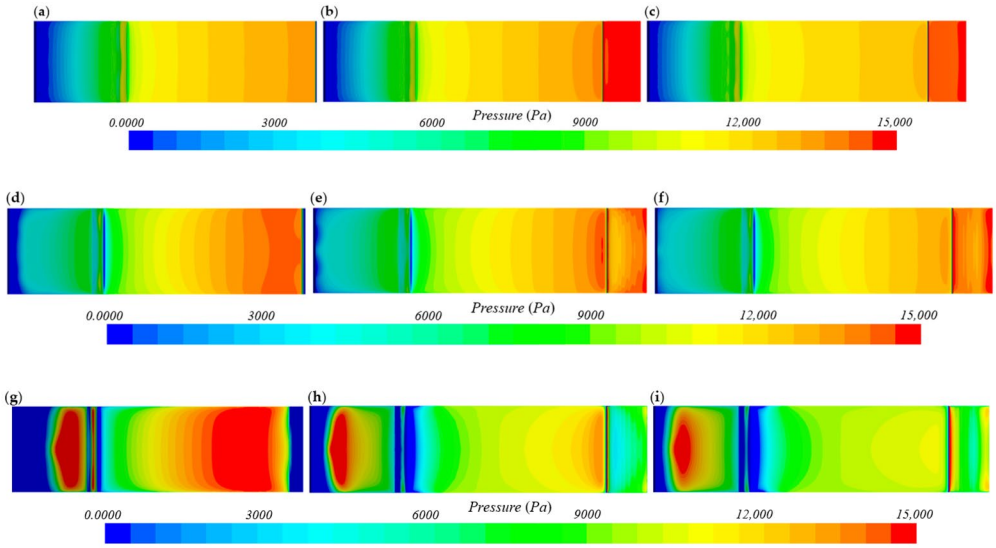

Figure 11. The underbody pressure distribution of typical speed conditions: (**a**) without hydrofoil Fr_{∇} = 0.43; (**b**) NACA0012 Fr_{∇} = 0.43; (**c**) NACA66-209 Fr_{∇} = 0.43; (**d**) without hydrofoil Fr_{∇} = 0.77; (**e**) NACA0012 Fr_{∇} = 0.77; (**f**) NACA66-209 Fr_{∇} = 0.77; (**g**) without hydrofoil Fr_{∇} = 1.3; (**h**) NACA0012 Fr_{∇} = 1.3; (**i**) NACA66-209 Fr_{∇} = 1.3.

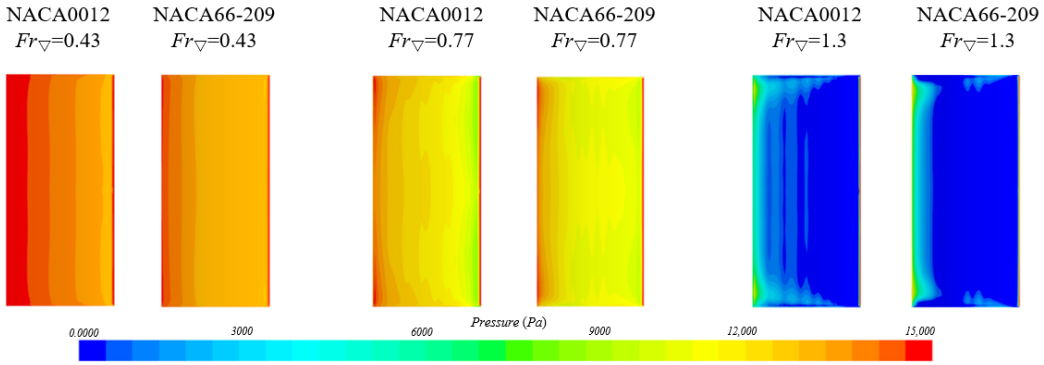

Figure 12. The pressure distribution on the upper surface of NACA0012 and NACA66-209 in typical speed conditions.

3.3. The Optimized Design of Hydrofoil NACA66-209 Based on Chord Lengths

For optimizing resistance reduction at medium and high speeds ($Fr_\nabla > 1$), the hydrofoil NACA66-209 was chosen for chord length optimization. The optimal tail wing chord length for the amphibious vehicle at $Fr_\nabla = 1.3$ was determined to achieve the lowest navigational resistance. This optimal chord length ensures the tail wing delivers the most effective resistance reduction.

An agent-based model optimization method [22] is utilized in this study to identify the optimal chord length (c) for the hydrofoil NACA66-209 equipped on an amphibious vehicle, aiming to achieve minimal sailing resistance at a Fr_∇ of 1.3. This methodology integrates numerical simulations with agent models, setting c as the variable under investigation, with the vehicle's resistance serving as the objective function. Resistance values for a range of c parameters are calculated through numerical simulations, creating a comprehensive dataset for optimization analysis. The process involves exploring this dataset to determine the c value that minimizes resistance, leveraging both numerical simulations and the construction of proxy models for accurate data representation. The selection of the optimal model is based on achieving the lowest possible error metrics, including the sum of squares error and the Prediction Error Sum of Squares (*PRESS*), which is expressed in Equation (6). Following the identification of the optimal chord length, further computational analysis is conducted to validate the optimization outcome.

$$PRESS = \sqrt{\frac{1}{N}\sum_{i=1}^{N}(y_i - y_i')^2} \tag{6}$$

where N is the number of sample points selected; y_i is the result of the numerical calculation of the resistance corresponding to the chord length c_i of the sample point, and y_i' is the fitted value of the resistance of the agent model at the chord length c_i.

This study investigated the amphibious vehicle's tail chord length (c) within a range of $0.313B$ to $0.937B$, selecting five points at intervals of $0.156B$ for resistance numerical calculations. Results, detailed in Table 6, reveal that resistance decreases and then increases with the tail chord length, indicating the optimal c lies between $0.781B$ and $0.937B$.

Table 6. The selection of tail wing chord length and numerical results of vehicle resistance.

Case	1	2	3	4	5
c (Chord Length)	$0.313B$	$0.469B$	$0.625B$	$0.781B$	$0.937B$
R_t/Δ	0.2038	0.1805	0.1591	0.1438	0.1475

Five proxy models, the polynomial response surface model (PRS), Kriging model (KRG), SHAP model (SHAP), and weighted average proxy model (WAS), were used to fit

the numerical results calculated in Table 6. There are 30 data points selected. The fitting results and fitting errors of each proxy model are shown in Figure 13.

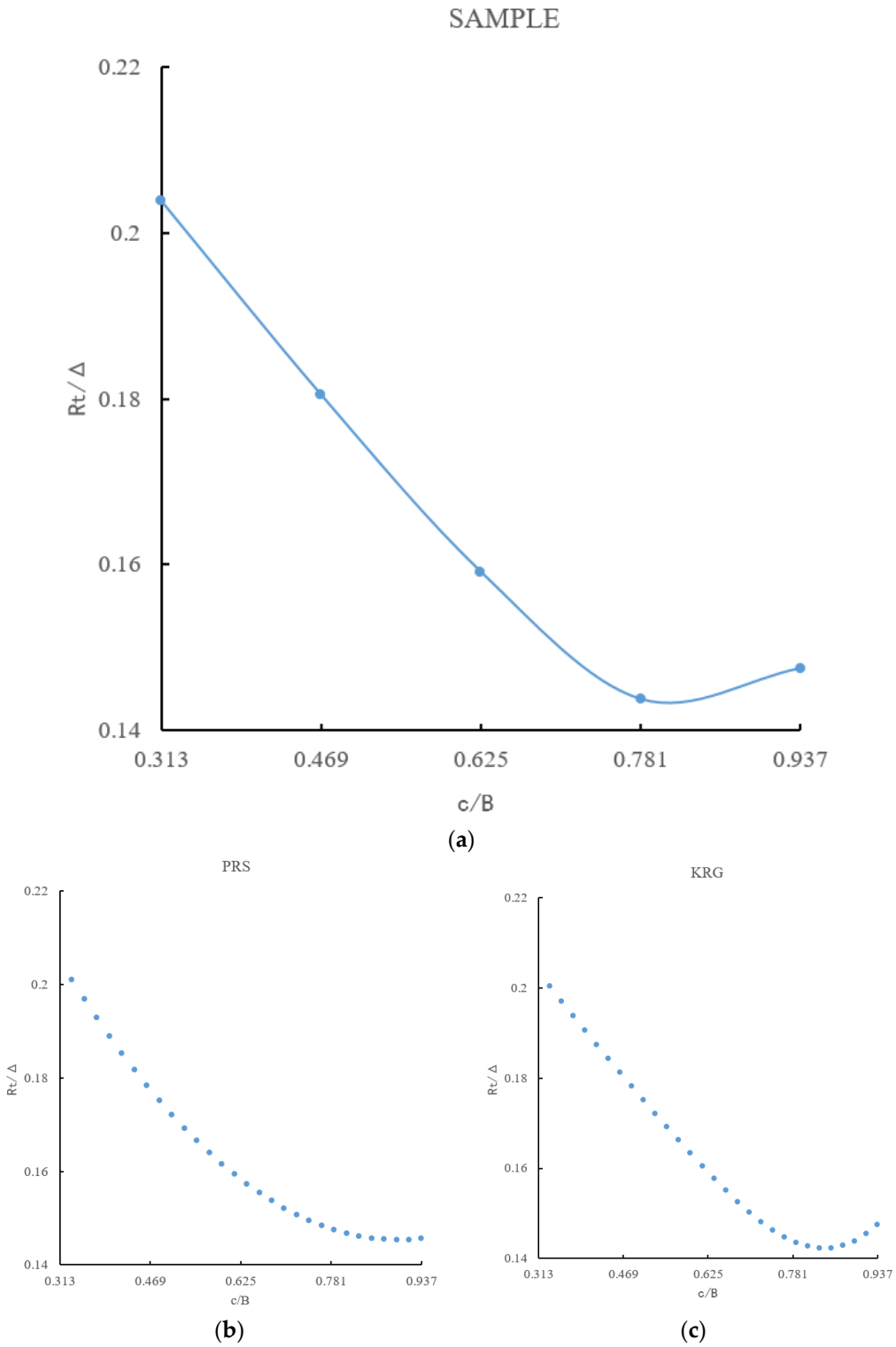

Figure 13. *Cont.*

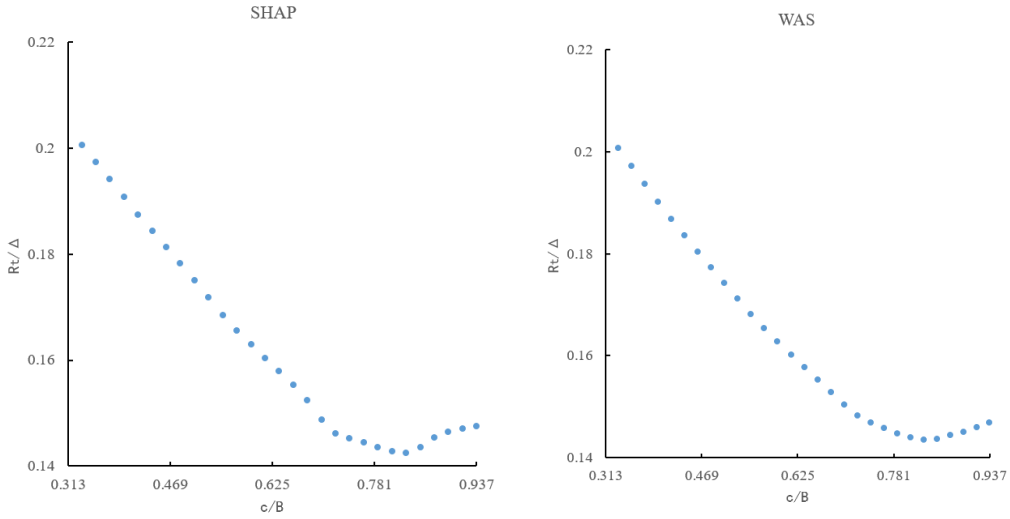

Figure 13. The chord length sample points and data fitting results of different proxy models: (**a**) sample; (**b**) PRS *PRESS* = 0.0101; (**c**) KRG *PRESS* = 0.0076; (**d**) SHAP *PRESS* = 0.0098; (**e**) WAS *PRESS* = 0.00074.

The proxy model that integrates data using a Weighted Allocation System (WAS) from three other models showed the lowest *PRESS*, with an error of 0.00074, making it the most accurate for optimizing the hydrofoil chord length. Utilizing WAS for single objective optimization, the optimal chord length was determined to be 0.83*B*, at which the amphibious vehicle's resistance is minimized, resulting in a R_t/Δ of 0.1422. This optimized chord length was further validated through CFDs simulations of the vehicle's resistance, with results presented in Table 7. The comparison confirmed that the discrepancy between the resistance coefficient derived from the WAS-optimized chord length and the CFDs simulation was under 1%, specifically an error value of 0.0013. This validation underscores the reliability and high accuracy of the optimization results achieved using the WAS proxy model.

Table 7. Optimization results and validation.

Method	R_t/Δ	Percentage Error (%)	Error
WAS	0.1435	0.9	0.0013
CFD	0.1422		

Selecting an optimized chord length of 0.83*B* for the amphibious vehicle's tail wing results in a 21.2% reduction in navigation resistance compared with the preoptimization model (NACA66-209 with a chord length of 0.469*B*). This demonstrates the significant impact of the tail wing's chord length on its resistance reduction capability, indicating that an appropriate hydrofoil chord length can markedly enhance the amphibious vehicle's resistance performance.

4. Conclusions

In this paper, CFDs methods and overset grid techniques are used to explore the resistance characteristics of amphibious vehicles equipped with various tail wings, including symmetrical hydrofoils (NACA0012, NACA0015, NACA0016) and asymmetric hydrofoils (NACA23012, NACA66-209), to identify the most effective tail wing shape for resistance reduction. The key findings and optimization results for the tail chord length under different sailing conditions ($0.43 < Fr_\nabla < 1.3$) are summarized as follows:

(1) At low speed (Fr_∇ = 0.43), adding a hydrofoil increases resistance by up to 18.2%. However, in transitional and high-speed sailing conditions (Fr_∇ > 0.9), the resistance reduction effect of the tail wing improves, exceeding 35% at Fr_∇ = 1.3. Thus, retracting the tail wing at low speeds and utilizing it at medium to high speeds is advisable for optimal performance.
(2) The vehicle's attitude changes significantly without a tail wing, with the tail inclination angle increasing with speed. Installing a tail wing moderates these changes, especially by reducing the tail inclination angle as speed increases.
(3) For symmetrical hydrofoils, increasing thickness worsens the resistance reduction effect at speeds higher than Fr_∇ = 1. This suggests that thicker symmetrical hydrofoils are less effective during transitional states.
(4) Asymmetric hydrofoils (NACA23012, NACA66-209) better improve the vehicle's sailing attitude, offering higher buoyancy and reduced tail inclination angles at medium to high speeds, leading to lower navigation resistance.
(5) The asymmetric hydrofoil NACA66-209 outperforms symmetrical hydrofoils in resistance reduction by 3–9% under medium and high speeds. While NACA23012 increases resistance at low speeds, NACA66-209 maintains similar low-speed resistance to symmetrical hydrofoils but significantly reduces resistance by up to 44.3% at higher speeds which is better than other hydrofoils.
(6) The tail wing selection and chord length optimization played an important role in enhancing amphibious vehicles' performance, particularly in transitioning from low to high-speed operations. The optimal chord length for NACA66-209 is determined to be 0.83B. Compared with the preoptimized model (NACA66-209 with a chord length of 0.469B), the optimized tail wing shows a further improvement in resistance reduction performance of 21.2%.

Author Contributions: Investigation, methodology, calculation, visualization, validation, formal analysis, and writing—original draft preparation, Z.J.; methodology and writing—review and editing, J.D. and Z.L. All authors have read and agreed to the published version of the manuscript.

Funding: This research received no external funding.

Institutional Review Board Statement: Not applicable.

Informed Consent Statement: Not applicable.

Data Availability Statement: Data is contained within the article.

Conflicts of Interest: The authors declare no conflicts of interest.

References

1. Kemp, J.A. Modeling and Simulation in Support of Operational Test and Evaluation for the Advanced Amphibious Assault Vehicle (AAAV). Ph.D. Thesis, Naval Postgraduate School, Monterey, CA, USA, 2001.
2. Latorre, R.; Arana, J. Reduction of Amphibious Vehicle Resistance and Bow Swamping by Fitting a Wave Cancellation Bow Plate. *Nav. Eng. J.* **2011**, *123*, 81–89. [CrossRef]
3. Yu, Z.Y.; Liao, Y.C.; Li, J.Y.; Ke, J. Simulation analysis of effect of different skateboard angles on lift-drag ratio of amphibious vehicle. *Ship Eng.* **2015**, *37*, 26–29.
4. Sun, C.; Xu, X.; Wang, W.; Xu, H. Influence on stern flaps in resistance performance of a caterpillar track amphibious vehicle. *IEEE Access* **2020**, *8*, 123828–123840. [CrossRef]
5. Du, Z.F.; Mu, X.L.; Li, Z.J. Numerical analysis of influence of stern flaps on motion and stability of high-speed amphibious platform. *Chin. J. Ship Res.* **2022**, *17*, 85–92.
6. Peng, K. Surrogate Based Optimization of Resistance Reduction of the Amphibious Vehicle. Master's Thesis, Beijing Institute of Technology, Beijing, China, 2015.
7. Lee, S.J.; Lee, T.I.; Lee, J.J.; Nam, W.; Suh, J.C. Hydrodynamic Characteristics of a Hydrofoil-assisted Amphibious Vehicle. *J. Ship Res.* **2017**, *61*, 15–22. [CrossRef]
8. Xu, H.; Xu, X.; Xu, L.; Liu, B. Sailing resistance reduction and speed raising for amphibious vehicles using novel configuration. *Sci. Sin.-Tech.* **2023**, *53*, 1272–1283. [CrossRef]
9. Liu, B.; Xu, X.; Pan, D.; Wang, X. Research on shipping energy-saving technology: Hydrofoil amphibious vehicle driven by waterjet propulsion. *J. Clean. Prod.* **2023**, *382*, 135257. [CrossRef]

10. Karelina, M.Y.; Filatov, V.V.; Klimov, A.V.; Malakhov, D.Y.; Sorokin, V.G. Marine propulsion study of planning small-class amphibious vehicles. *IOP Conf. Ser. Mater. Sci. Eng.* **2020**, *832*, 012007. [CrossRef]
11. Liu, B.; Xu, X.; Pan, D. Influence of resistance due to locomotion mechanism configurations of a new high-speed amphibious vehicle (HSAV-II). *Ocean Eng.* **2023**, *283*, 115175. [CrossRef]
12. Pan, D.; Xu, X.; Liu, B. Influence of Flanks on Resistance Performance of High-Speed Amphibious Vehicle. *JMSE* **2021**, *9*, 1260. [CrossRef]
13. Pan, D.; Xu, X.; Liu, B.; Xu, H.; Wang, X. A review on drag reduction technology: Focusing on amphibious vehicles. *Ocean Eng.* **2023**, *280*, 114618. [CrossRef]
14. Doctors, L.J. Hydrodynamics of transom-stern flaps for planing boats. *Ocean Eng.* **2020**, *216*, 107858. [CrossRef]
15. Lee, D.; Ko, S.; Park, J.; Kwon, Y.C.; Rhee, S.H.; Jeon, M.; Kim, T.H. An Experimental Analysis of Active Pitch Control for an Assault Amphibious Vehicle Considering Waterjet-Hydrofoil Interaction Effect. *JMSE* **2021**, *9*, 894. [CrossRef]
16. Liu, B.; Pan, D.; Xu, X. Research on the resistance and maneuvering characteristics of an amphibious transport vehicle and the influence of stern hydrofoil. *Ocean Eng.* **2024**, *293*, 116592. [CrossRef]
17. Dwiputera, H.; Prawira, N.Y.; Andira, M.A.; Budiyanto, M.A. Effect of Angle of Attack Variation of Stern Foil on High-Speed Craft on Various Speed with Computational Fluid Dynamics Method. *Int. J. Technol.* **2020**, *11*, 1359–1369. [CrossRef]
18. Ganesan, S.; Esakki, B. Computational fluid dynamic analysis of an unmanned amphibious aerial vehicle for drag reduction. *Int. J. Intell. Unmanned Syst.* **2020**, *8*, 187–200. [CrossRef]
19. Dhana, F.R.; Park, J.C.; Yoon, H.K. A Numerical Study on the Influence of Caterpillars to the Resistance Performance of an Amphibious Vehicle. *JMSE* **2023**, *11*, 286. [CrossRef]
20. Zhou, L.; Zhang, L. Numerical Study on Sailing Resistance Characteristics of Amphibious Vehicle. *J. South China Univ. Technol.* **2021**, *49*, 133–142.
21. International Towing Tank Conference (ITTC). The specialist committee on CFD in marine hydrodynamics-recommended procedures and guidelines: Practical guidelines for ship CFD application. In Proceedings of the 26th ITTC, Rio de Janeiro, Brazil, 28 August–3 September 2011.
22. Queipo, N.V.; Haftka, R.T.; Shyy, W.; Goel, T.; Vaidyanathan, R.; Tucker, P.K. Surrogate-based analysis and optimization. *Prog. Aerosp. Sci.* **2005**, *41*, 1–28. [CrossRef]